Minimum stopping distance on split friction roads via joint control of steering and individual wheel braking

Taylor & Francis
Taylor & Francis Group

Vehicle System Dynamics
International Journal of Vehicle Mechanics and Mobility

ISSN: 0042-3114 (Print) 1744-5159 (Online) Journal homepage: www.tandfonline.com/journals/nvsd20

Minimum stopping distance on split friction roads via joint control of steering and individual wheel braking

Ektor Karyotakis, Mats Jonasson, Derong Yang & Jonas Sjöberg

To cite this article: Ektor Karyotakis, Mats Jonasson, Derong Yang & Jonas Sjöberg (01 Mar 2026): Minimum stopping distance on split friction roads via joint control of steering and individual wheel braking, Vehicle System Dynamics, DOI: 10.1080/00423114.2026.2630033

To link to this article: https://doi.org/10.1080/00423114.2026.2630033

Published online: 01 Mar 2026.

VEHICLE SYSTEM DYNAMICS
https://doi.org/10.1080/00423114.2026.2630033

Minimum stopping distance on split friction roads via joint control of steering and individual wheel braking

Ektor Karyotakis [a,b], Mats Jonasson [c], Derong Yang[a] and Jonas Sjöberg[b]

[a]Vehicle Energy and Motion Control, Volvo Car AB, Gothenburg, Sweden; [b]Department of Electrical Engineering, Chalmers University of Technology, Gothenburg, Sweden; [c]Department of Maritime and Mechanical Engineering, Chalmers University of Technology, Gothenburg, Sweden

ABSTRACT

This paper examines the problem of minimising stopping distance on split friction roads by joint control of individual wheel brakes and automated steering. A static optimisation problem is introduced that maximises braking on split friction roads without veering out-of-lane. The analysis of the optimal brake forces and counter-steering shows different properties of the optimal solution depending on the degree of split friction assymmetry between the left and right vehicle sides. The solutions are categorised into two regions: small and large split friction asymmetries. At a small split friction asymmetry, all the tyres are at their force peak in their force-slip curves and the slips are small. Therefore, the traditional ABS and a path-following controller give optimal braking and path deviation performance. Whereas at a large split friction asymmetry, it is shown that having all tyres at their force-slip peak is impossible. Instead, allowing larger slips at the low-friction tyres gives maximum braking. Surprisingly, constraining slip constraint on one low-friction tyre limits the available tyre force on the high-friction ones, ultimately leading to longer stopping distances. For braking at large splits, we propose using optimal static solutions to set a feedforward steering angle based on the split friction condition, together with a high-friction brake control to the yaw torque. This control framework is tested in vehicle simulation in the CarMaker environment. Closed-loop simulations of the proposed control framework are compared to an emulated driver response derived from measurements of a professional driver. Stopping distance gains of 6–13% are observed by automating the steering compensation. Further simulations demonstrate that the proposed control framework provides maximum braking even when one side has zero friction.

ARTICLE HISTORY
Received 27 September 2024
Revised 4 July 2025
Accepted 5 February 2026

KEYWORDS
Split friction; stopping distance minimisation; brake optimisation; friction asymmetry; counter-steering; Lyapunov control

1. Introduction

Split friction is a special case of a slippery road when one side of the vehicle lies on a low-friction patch, such as snow or oil spillage, while the other is on high-friction asphalt. When braking hard on split friction, the larger braking forces on the high-friction side create a yaw torque disturbance, which can cause the vehicle to start rotating. The driver can

CONTACT Ektor Karyotakis ektor.karyotakis@volvocars.com

compensate by counter-steering, but it requires some skills. The compensation can be done instead through an advanced driver-assistance system (ADAS) function to assist or replace the driver. Potentially, the ADAS function can be made better than most drivers.

Analysis of NHTSA's crash data from 2018–2020 shows an average of 1160 fatal U.S. crashes per year involving braking and skidding before impact [1]. Since skidding often occurs on split friction roads, the proposed function could help prevent a portion of these incidents.

In a previous study [2], drivers were subjected to automated emergency braking (AEB) on split friction. Distracted drivers took longer to react, potentially departing from the lane. Automated steering compensation can enhance safety and reduce workload for non-distracted drivers. Recent publications [3–5] focus on designing a steering controller to assist the driver, assuming the ABS handles braking. In [3], a sliding mode controller is designed for robustness against parameter uncertainties. In [4,5], receding horizon LQR control is used for steering compensation, considering deviations from the predicted path. These works assume the ABS system manages braking, with the steering controller providing counter torque to compensate for brake-induced torque. However, our analysis shows this approach is only optimal for small split friction. For large split friction, where friction is very low on one side, the optimal solution requires a more elaborate control structure.

Previous studies combined steering compensation and brake control. Paper [6] challenged the assumption that ABS controls the brakes, introducing a multivariable controller to maintain wheel slips before the peak slip region, while preserving lateral stability through steering. We will show that maintaining slip in the linear region is suboptimal at large split frictions. In [7], an MPC-based controller integrated steering and braking to achieve optimal deceleration for a bus. The control strategy relied on a predefined yaw acceleration threshold to switch between control modes, which would require the vehicle to rotate before an adaptation could occur. In contrast, this paper employs an estimate of the road's split friction to select the appropriate control mode, enabling immediate activation upon braking. Moreover, [7] constrained the high-friction tyres to the linear region and did not investigate control performance under large splits, which are explicitly considered in this work.

In previous work [8], we used static optimisation to show that counter-steering is required for optimal braking on split friction surfaces, depending on the split friction asymmetry. This study extends that analysis by (1) examining optimal solutions beyond peak slip, and (2) proposing a control strategy to maintain the vehicle near this optimum despite varying conditions or disturbances. The controller's ability to remain close to this optimum is demonstrated through simulations using a high-fidelity CarMaker^{TM} vehicle model.

This work proposes a control strategy tailored for high split-friction conditions, comprising a constant feedforward steering input derived from the static analysis (stored in an offline lookup table) and a dynamic feedback component that controls high-friction side braking to reduce excessive yaw torque. Furthermore, a lateral controller is integrated to prevent lane departures, an aspect not thoroughly addressed in the referenced literature. The complete framework is benchmarked against an emulated state-of-the-art ABS controller based on professional driver measurements.

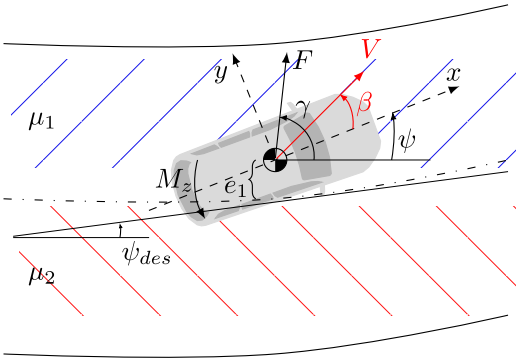

Figure 1. Vehicle in road lane, along with the velocity, force, and torque at CoG and their orientations.

2. Problem definition

2.1. Road description

Figure 1 shows the road friction condition, lane borders, and vehicle relative to the lane centreline. The left and right sides of the lane have different friction, $[\mu_1, \mu_2]$ and the *friction asymmetry* is defined as

$$\Delta_\mu = \mu_1 - \mu_2 \tag{1}$$

2.2. Vehicle trajectory and orientation

Assuming the vehicle is a rigid body, its trajectory is defined by the sum of the applied forces and torques. The vehicle's trajectory is described by the *velocity vector* V, the *total force* F, and *yaw torque* M_z acting in its centre of gravity (CoG), presented in Figure 1. The vehicle's direction is defined by the *yaw angle* ψ. The *body slip angle* is the angle between the direction of the vehicle and the velocity vector

$$\beta = \arctan\left(\frac{v_y}{v_x}\right) \tag{2}$$

where v_x and v_y are the projections of V to the x and y axes of the body, respectively.

Similarly, the *force angle* is defined as

$$\gamma = \arctan\left(\frac{F_y}{F_x}\right) \tag{3}$$

where F_x and F_y are the projections of F to the x and y axes of the body, respectively.

It is often convenient to rotate the forces along the velocity direction as

$$\begin{pmatrix} F_v \\ F_p \end{pmatrix} = \begin{pmatrix} \cos\beta & \sin\beta \\ -\sin\beta & \cos\beta \end{pmatrix} \begin{pmatrix} F_x \\ F_y \end{pmatrix} \tag{4}$$

where F_v is the force along and F_p perpendicular to the velocity vector V.

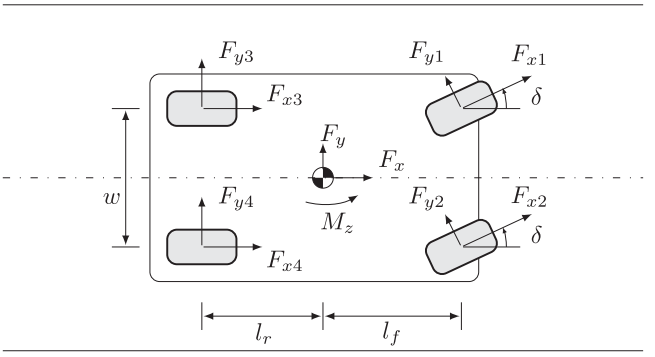

Figure 2. Double-track vehicle model with front-wheel steering.

Using a force-centric approach (as in [9]), achieving the shortest stopping distance is equivalent to minimising F_v, the force opposite to the velocity, at every time instant. Further, the yaw torque M_z should be zero to avoid vehicle rotation. Finally, for braking in a straight line, the force perpendicular to the velocity F_p should also be zero to avoid lateral deviation. This idealised objective can be expressed as the following conceptual optimisation problem (OP)

$$\begin{aligned} \min \quad & F_v \\ \text{s.t.} \quad & F_p = 0 \\ & M_z = 0 \end{aligned} \tag{5}$$

While this formulation captures the high-level goal, the actual objective – detailed later in (29) – must account for the fact that F and M_z are derived from the combined forces at the four tyres, which are functions of the applied braking and steering inputs. This relationship between individual tyre forces and the resulting global forces is detailed in the following section, where the vehicle model is introduced.

3. Vehicle model

3.1. Double-track vehicle model

This section describes the double-track model used to examine the brake force and steering allocation in a split friction braking manoeuvre. The following assumptions are made: (a) Differential braking, where each wheel brakes independently. (b) Front-wheel steering. (c) Neglecting pitch and roll dynamics. (d) Assuming a flat ground. (e) Straight driving, for presentation simplicity.

Figure 2 illustrates the notation of the vehicle model and the tyre forces. The tyre forces are typically modelled as functions of their slip. Especially the lateral forces significantly depend on the *steering angle* δ. The tyre force-slip relation will be defined in Section 3.2.

From Figure 2, the total force at the CoG F is divided into the longitudinal F_x and lateral forces F_y. The forces F_x and F_y and the yaw moment M_z about the vertical axis are given

by

$$\begin{aligned} F_x &= (F_{x1} + F_{x2})\cos\delta - (F_{y1} + F_{y2})\sin\delta + F_{x3} + F_{x4} \\ &\approx (F_{x1} + F_{x2} + F_{x3} + F_{x4}) - (F_{y1} + F_{y2})\,\delta \end{aligned} \tag{6}$$

$$\begin{aligned} F_y &= (F_{x1} + F_{x2})\sin\delta + (F_{y1} + F_{y2})\cos\delta + F_{y3} + F_{y4} \\ &\approx (F_{y1} + F_{y2} + F_{y3} + F_{y4}) + (F_{x1} + F_{x2})\,\delta \end{aligned} \tag{7}$$

$$\begin{aligned} M_z &= ((F_{x1} + F_{x2})\sin\delta + (F_{y1} + F_{y2})\cos\delta)\cdot l_f \\ &\quad - (F_{y3} + F_{y4})\cdot l_r \\ &\quad + ((-F_{x1} + F_{x2})\cos\delta + (F_{y1} - F_{y2})\sin\delta - F_{x3} + F_{x4})\cdot \frac{w}{2} \\ &\approx M_\delta - M_{\Delta F_x} + M_{cross} \end{aligned} \tag{8}$$

where a small δ assumption is used. The terms $[M_{\Delta F_x}, M_\delta, M_{cross}]$ are yaw torque contributions due to braking, steering, and a cross-term, respectively, given by

$$M_{\Delta F_x} = ((F_{x1} + F_{x3}) - (F_{x2} + F_{x4}))\frac{w}{2} \tag{9}$$

$$M_\delta = (F_{y1} + F_{y2})l_f - (F_{y3} + F_{y4})l_r \tag{10}$$

$$\begin{aligned} M_{cross} &= (F_{x1} + F_{x2})l_f\,\delta + (F_{y1} - F_{y2})\frac{w}{2}\,\delta \\ &\approx (F_{x1} + F_{x2})l_f\,\delta \end{aligned} \tag{11}$$

The equations of motion of the vehicle are decomposed into a translation and a rotation part of the body and are expressed by

$$\dot{v}_x = a_x + v_y\dot{\psi} = \frac{F_x}{m} + v_y\dot{\psi} \tag{12}$$

$$\dot{v}_y = a_y - v_x\dot{\psi} = \frac{F_y}{m} - v_x\dot{\psi} \tag{13}$$

$$\ddot{\psi} = \frac{M_z}{I_{zz}} \tag{14}$$

where the forces and moments from (6)–(8) are used. A detailed derivation of (12)–(14) is given in [9].

Equations (12)–(14) describe the vehicle's motion as a function of the steering and brake forces at each individual wheel. Hence, by controlling the steering and braking, these equations describe the vehicle's longitudinal-, lateral speed, and its rotation.

Next, the relation of the tyre forces to slip and available friction are presented.

3.2. Tyre model for combined slip

This section explains how the tyre forces depend on the slip and available tyre-road friction. It also describes how the longitudinal and lateral forces affect each other, referred to as the *combined slip*.

Slip is the relative movement between the tyre's contact patch and the road. Definitions of slip are given first in the longitudinal and lateral directions, assuming no interaction with one another.

The *longitudinal slip ratios* are defined as

$$\kappa_i = \frac{R_w \omega_i - v_{xi}}{v_{xi}} \tag{15}$$

where ω_i is the wheel speed, R_w is the tyre radius, and $i \in \{1, 2, 3, 4\}$ for each tyre as in Figure 2.

The *lateral slip angles* are defined as

$$\alpha_i = -\arctan \frac{v_{yi}}{v_{xi}} \tag{16}$$

The velocity vectors of each wheel (v_{xi}, v_{yi}) used in (15) and (16) are obtained by a rotational transformation of the vehicle speed $[v_x,\ v_y]$ as

$$\begin{pmatrix} v_{xi} \\ v_{yi} \end{pmatrix} = \begin{pmatrix} \cos\delta & \sin\delta \\ -\sin\delta & \cos\delta \end{pmatrix} \begin{pmatrix} v_x - \dot{\psi}\, l_{yi} \\ v_y + \dot{\psi}\, l_{xi} \end{pmatrix} \tag{17}$$

where the distances of the CoG to the front/rear axles are $l_{xi} = [l_f, l_f, -l_r, -l_r]^\intercal$, and the distances of the CoG to the left/right vehicle sides are $l_{yi} = \frac{w}{2}[1, -1, 1, -1]^\intercal$.

Equations (15) and (16) describe the tyre slip in case of *either* braking or steering. Since combined braking and cornering is considered, the combined slip at each wheel is needed, as described in [10, Chapter 13]. It is defined by combining the *longitudinal slips*

$$\sigma_{xi} = \frac{\kappa_i}{1 + \kappa_i} \tag{18}$$

and the *lateral slips*

$$\sigma_{yi} = \frac{\tan\alpha_i}{1 + \kappa_i} \tag{19}$$

leading to the *combined slips*

$$\sigma_i = \sqrt{\sigma_{xi}^2 + \sigma_{yi}^2} \tag{20}$$

Using the combined slip, the magnitude of the *tyre forces* F_i, which can be seen as combining F_{xi} and F_{yi} for each tyre, is modelled with a simplified Magic Formula (adapted from [11]) as

$$F_i = F_{\max,i} \sin\left[C \arctan\left(\frac{K_i \sigma_i}{C\, F_{\max,i}}\right)\right] \tag{21}$$

where K_i are the tyre stiffness, C is a shape factor at large slip, and $F_{\max,i}$ are the *maximum attainable forces*, defined as

$$F_{\max,i} = \mu_i F_{zi} \tag{22}$$

with μ_i the friction coefficient and F_{zi} the vertical force of each tyre. The F_{zi} are obtained from a steady state longitudinal- and lateral load transfer model, as in [12, p. 350]. Further,

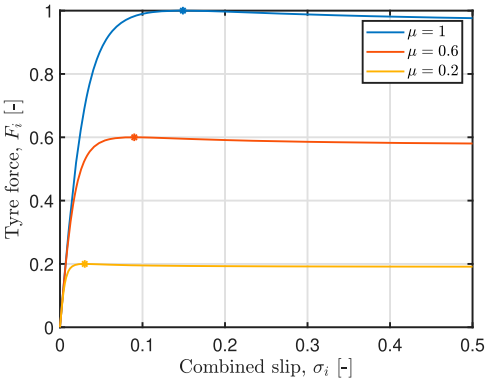

Figure 3. Normalised tyre force-slip curve; $C = 1.2$ [–] & $K = 30$ [–].

K_i is assumed to be linearly dependant on F_{zi}. The tyre force F_i as a function of the combined slip σ_i is presented in Figure 3 and shows how the curve changes with the friction coefficient μ. In the figure, the asterisks depict the $F_{\max,i}$, which happens at the *peak slip*, obtained from inverting the tyre model (21) as

$$\sigma_i^* = \tan\left[\frac{1}{C}\arcsin(1)\right]\frac{C F_{\max,i}}{K_i} \tag{23}$$

The longitudinal and lateral tyre forces can then be described as

$$F_{xi} = \frac{\sigma_{xi}}{\sigma_i}F_i \tag{24}$$

$$F_{yi} = \frac{\sigma_{yi}}{\sigma_i}F_i \tag{25}$$

$$F_i = \sqrt{F_{xi}^2 + F_{yi}^2} \tag{26}$$

The *friction circle* describes the tyre limits as

$$F_i \leq F_{\max,i} \tag{27}$$

The tyre force at a particular tyre is on the friction circle when $F_i = F_{\max,i}$ and $\sigma_i = \sigma_i^*$, i.e. when the slip is optimal. The friction circle is already incorporated in the mathematical description of the combined tyre model (24) and (25) by the definition of F_i in (26), and does not need to be imposed as a constraint in the upcoming optimisation problem.

This section showed the relation of the tyre forces, vehicle states (velocities and yaw rate), and steering angle at an individual tyre level. Next, an optimisation problem is set up, connecting the (a) tyre forces, (b) vehicle states, (c) steering angle, and (d) friction to the (e) global forces from (4). By varying the friction (d) difference between the vehicle sides, its effect on the others [(a)–(c), (e)] is revealed.

4. Static solution for maximum deceleration on split friction

This section uses the established mathematical description from the previous section to find the brake force and counter-steering allocation that gives the shortest stopping distance depending on the split friction.

Two formulations of the static optimisation problem are considered and compared. The *High-slip Optimum* (HsO) represents the ideal braking equilibrium obtained without slip constraints, allowing tyres to operate beyond peak slip. In contrast, the *Low-Slip* (LS) solution reflects a constrained case aligned with production ABS behaviour, where slip levels are limited to ensure stability.

We consider the *static* solution, meaning that the problem is simplified by removing the dynamics. It was first introduced in [8] and is briefly explained next.

The high-level OP (5) is updated with the expressions for (F_v, F_p) from (4). In (4), the (F_x, F_y) are replaced from (6) and (7), which depend on the tyre forces (F_{xi}, F_{yi}), obtained from the tyre model (24) and (25). The yaw torque constraint ($M_z = 0$) is equivalent to setting the yaw acceleration $\ddot{\psi}$ to zero. The yaw rate $\dot{\psi}$ is also put to zero for straight roads. The yaw rate ($\dot{\psi} = 0$) constraint reduces the lateral slip angles from (16) and (17) to a function of β and δ as

$$\tan \alpha_i = [\delta - \beta, \delta - \beta, -\beta, -\beta]^\intercal \tag{28}$$

Then, the combined slip expressions (18)–(20) become a function of the optimisation variables $q = [\kappa_i, \delta, \beta]^\intercal$. β and $\dot{\psi}$ are the states, while κ_i and δ are the control variables for the brakes and steering, respectively. The control framework, which brings the vehicle to and maintains it at the optimal state, is discussed in Section 5. Combined braking and steering have two major effects at the vehicle level: vertical load transfer and vehicle rotation by β, making the determination of control variables an optimisation problem.

The maximum static deceleration optimisation problems (LS and HsO) for a straight road become

$$\begin{aligned} \min_{q} \quad & a_v(q) \\ \text{s.t.} \quad & F_p(q) = 0 \\ & M_z(q) = 0 \\ & \dot{\psi} = 0 \\ & h_i(q) \leq 0 \end{aligned} \tag{29}$$

where the low-slip constraints

$$h_i = \sigma_i(q) - \sigma_i^* \tag{30}$$

are included for the LS but excluded for the HsO. Further, $a_v = \frac{1}{m} F_v$, and σ_i^* is the peak slip from (23).

The motivation for the LS constraint h comes from production ABS systems, which often include mechanisms to prevent rear wheel slip from exceeding front wheel slip for stability reasons [13]. Similarly, [14] describes a 'select-low' strategy, where equal torque is applied to both rear wheels to limit slip. While such constraints enhance stability, they also limit braking performance under large split friction conditions–particularly by restricting

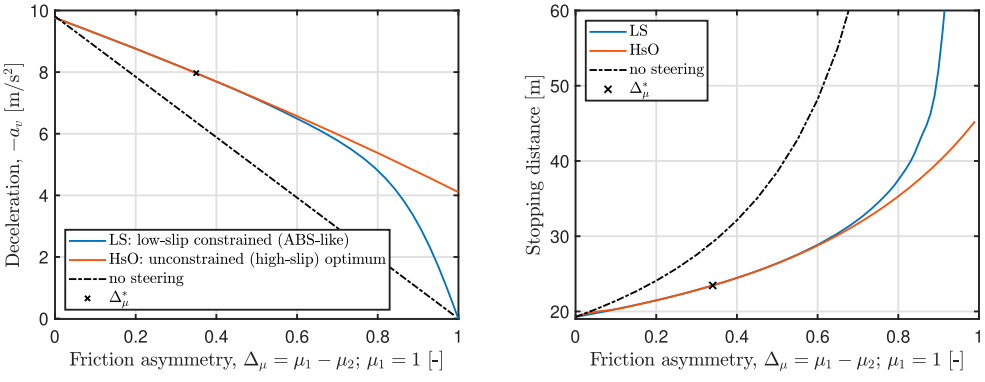

(a) Deceleration (b) Stopping distance for $v_{x0} = 70$ km/h

Figure 4. Deceleration and stopping distance vs friction asymmetry for the optimal static solution when braking in a straight line. Three optimal solutions are presented depending on whether the steering or the low-slip constraint is active. At Δ_μ^* the LS and HsO solutions diverge. (a) Deceleration (b) Stopping distance for $v_{x0} = 70$ km/h.

the high-friction side. This trade-off is explored in the following section, where the impact of the LS constraint on braking performance is analysed.

The optimisation problems (29) (LS and HsO) give the brake forces and steering angle inputs that make the vehicle brake as hard as possible without rotation (referred to as the optimal solutions). Next, the optimal solutions are analysed as a function of the friction asymmetry. The purpose of this analysis is to inspire control principles.

4.1. Optimal solution in a straight line

This section examines the maximum deceleration, the tyre force-slip curves, and the steering angles of each optimal solution.

The nonlinear optimisation solver *fmincon* of Matlab^{TM} is used for a range of Δ_μ values with $\mu_1 = 1$ and $\mu_2 \in [1, 0.01]$, and the results are presented in Figure 4. Here, the left vehicle side is chosen as the high-friction one. Figure 4(a) presents the maximum deceleration. Setting $\delta = 0$ in the OP, the brake forces become equal per axle, resulting in zero yaw torque but this gives less deceleration, presented in the figure with a dash-dotted black line. The LS solution (with the low-slip constraint h) is presented with a solid blue line, and the HsO (optimum, without h) is presented with a solid red line.

The deceleration curves from Figure 4(a) are transformed into stopping distance, assuming the deceleration is constant, and for an initial speed $v_{x0} = 70$ km/h the results are presented in Figure 4(b). The stopping distances for LS and HsO are quite similar up to $\Delta_\mu = 0.8$. For larger splits, there is a significant gain with the HsO solution. For example, for $\Delta_\mu = 0.9$, the stopping distance is roughly 12.5 m or, equivalently, 25% shorter. In the extreme case of black ice, i.e. no friction on one vehicle side, the LS does not provide any braking at all. The tyre force-slip details of the two solutions are explained next.

Figure 5 shows how constraining the slip affects the tyre forces for two Δ_μ values, (a) at a small and (b) at a large split friction asymmetry. For the small split case (Figure 5(a)), the forces are at their peak, and the slip is equal to the peak slip σ^*, for both the LS and

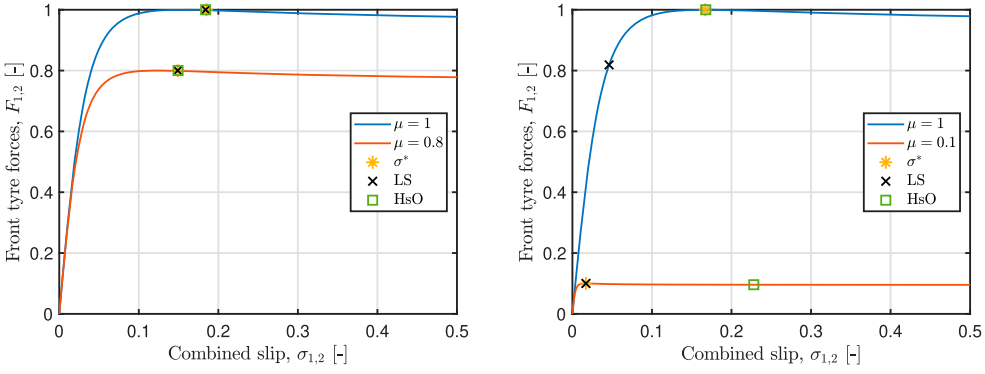

(a) Small split friction asymmetry; $\Delta_\mu = 0.2$ (b) Large split friction asymmetry; $\Delta_\mu = 0.9$

Figure 5. Normalised tyre force vs slip curves for the front tyres (similar tendencies occur in the rear tyres). The markers correspond to force for the peak slip σ^* and the optimal solutions with (LS) and without (HsO) the low-slip constraint. (a) Small split friction asymmetry; $\Delta_\mu = 0.2$ (b) Large split friction asymmetry; $\Delta_\mu = 0.9$.

HsO. Thus, all forces are on the friction circle, as $F_i = F_{\max,i}$. For the large split case on the other hand (Figure 5(b)), it is not possible to have both the forces on the high- and the low-friction side at their peak values. The HsO solution reveals that the low-friction tyres must have larger-than-the-peak slips for maximum braking at large split friction asymmetries. Since the slips in each axle are similar due to steering from (28), the LS is constrained close to the low-friction tyre peak. Without the slip constraint, more counter-steering can be applied, which increases the lateral slip, but also the tyre force, and hence gives harder braking. Part of this tyre force is for steering and part is for braking. The resultant force vectors are illustrated in Figure 7(b,c).

From this discussion, we claim that at large splits:

- With a slip constraint on any low-friction tyre, only part of the possible friction force is obtained at the high-friction tyres.
- Since the low-friction tyres are in the unstable sliding region, the low-friction side's contribution can be disregarded from controlling the vehicle's yaw torque and total force.

We introduce the friction asymmetry value Δ_μ^* to indicate at which split value the LS and HsO solutions start to diverge.

Definition 4.1: The Δ_μ^* is the friction asymmetry value in the OP that any tyre's slip σ_i changes from the optimal σ_i^* by a percentage ϵ. That is expressed mathematically as

$$\Delta_\mu^* = \left\{ \Delta_\mu \mid \frac{|\sigma_i - \sigma_i^*|}{\sigma_i^*} \leq \epsilon, \text{for any} i \in [1,2,3,4] \right\} \tag{31}$$

The precise value of ϵ is not crucial, it can be seen as numerical precision in deciding upon Δ_μ^* Here $\epsilon = 10\%$ is chosen.

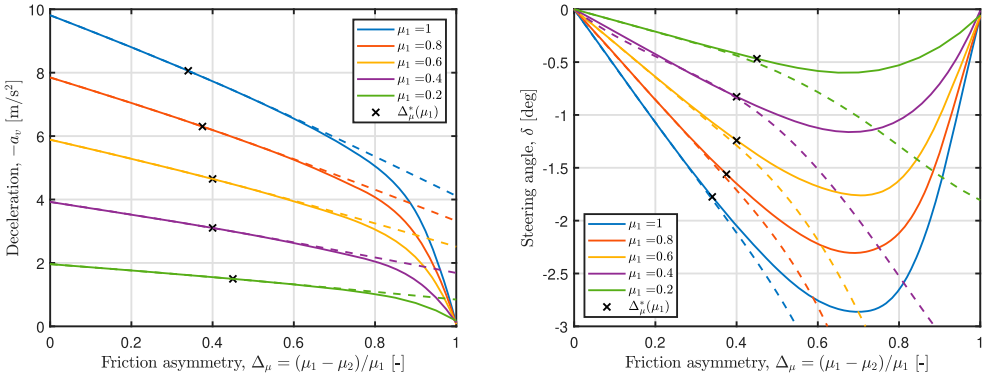

(a) Deceleration (b) Steering angle

Figure 6. Deceleration and steering angle vs friction asymmetry for the optimal solution for several high-friction side values μ_1. Solid lines represent the LS solution and dashed the HsO solution. (a) Deceleration (b) Steering angle.

The Δ^*_μ point depends on the high-friction road friction coefficient μ_1, as illustrated in Figure 6. The lines represent solutions to the OP (29) with (LS) and without (HsO) the low-slip constraint h, solved with $\mu_1 \in [1, 0.2]$ and $\mu_2 \in [\mu_1, 0.01]$. Figure 6(a) presents the deceleration and shows that the solution characteristics also depend on how slippery the high-friction side is. This knowledge should be considered in the control design.

Figure 6(b) provides the optimal steering angle based on the road condition and indicates the relation between steering and maximum braking. The steering angle peaks for a $\Delta_\mu > \Delta^*_\mu$ for the LS. For the HsO on the other hand, the steering angle drastically increases its gradient at $\Delta_\mu = \Delta^*_\mu$. The drawback with the LS condition is also visible here as progressively less counter-steering is used at large splits, and totally disappears at $\Delta_\mu = 1$.

Summing up, the optimal solution analysis reveals two regions based on the split friction asymmetry with different solution characteristics. The following section presents the optimal brake force and steering allocations.

4.2. Brake & steering allocation at small/large split friction asymmetries

This section investigates further the properties of the LS and HsO solutions by analysing what the optimal brake forces and steering look like in the vehicle. This analysis gives insights into the yaw controller and how the results can be extended to non-straight braking in a curve.

Figure 7 shows the vehicle's optimal tyre forces and counter-steering in the two regions, small and large split friction. At small split friction asymmetry ($\Delta_\mu < \Delta^*_\mu$), all tyres are saturated: in Figure 7(a), the tyre forces touch the friction circle. At large split friction asymmetry ($\Delta_\mu > \Delta^*_\mu$), the tyre forces and steering vary between the two solutions (LS and HsO). The low-friction tyres are saturated for both cases. For the LS solution, in Figure 7(b), the high-friction tyres are far from the friction circle. That comes as the high-friction tyres reduce braking due to the counter-steering being limited by the slip constraint at the low-friction side. As presented in Figure 5, increasing counter-steering increases slip and

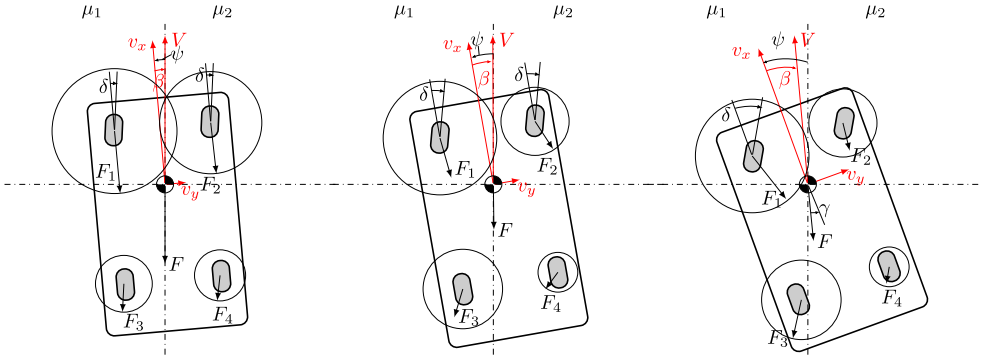

(a) Small split (b) Large split: LS (c) Large split: HsO

Figure 7. Optimal tyre force distribution and counter-steering at small and large split friction asymmetry. The friction circles are scaled with the vertical load. $\mu_1 > \mu_2$. The angles are exaggerated for viewing purposes.

violates the low-slip constraint. For the HsO (Figure 7(c)), the tyres on the high-friction side obtain peak slip, giving maximum forces on the friction circle. However, on the low-friction side, the forces are lower than the maximum value, as the tyres are sliding. A further implication of the high slip values on the low-friction side is that the steering angle has close to no influence on these tyre forces.

The optimal braking problems (29) are formulated with a torque constraint ($M_z = 0$) which prevents the vehicle from rotating. In real-time, a yaw controller achieves this. Further, the constraint $F_p = 0$ ensures the vehicle does not move laterally to the path, and a path controller controls the yaw direction to comply with this constraint. The consequence of applying these two constraints on a straight road is that the body is tilted at steady-state by a yaw angle equal to the body slip angle, i.e. $\psi = -\beta$. The body slip angle is generally small, as shown in the simulations of Section 7. However, to rotate the body by β, an initial transient phase of building up the brake forces and steering angle is needed giving transients in both the yaw torque and the lateral position.

Due to $F_p = 0$, the optimal direction of the total force F is opposite to the velocity vector V, i.e. $\gamma = 180^\circ - \beta$. The straight-road condition $F_p = 0$ can easily be changed if the vehicle travels in a curve. Then F_p should instead have the value determined by the local curvature and the speed.

Next, the details of choosing a larger-than-optimal steering wheel angle are discussed.

4.3. Counter-steering saturation and maximum braking at large split

Before transitioning from the static maximum braking solution to the control strategies, we will analyse the system properties for steering angles near the optimum. Specifically, we focus on the balance between counter-steering and brake torque to maintain the vehicle's yaw direction.

At extreme friction asymmetries, the low-friction tyres are ineffective as they are in the unstable sliding region and provide negligible friction force, as shown in Figure 5(b). Therefore, the contribution of the low-friction tyres is disregarded. Instead, this analysis focuses on the high-friction brake M_{Fxh} and steering torque M_δ equilibrium.

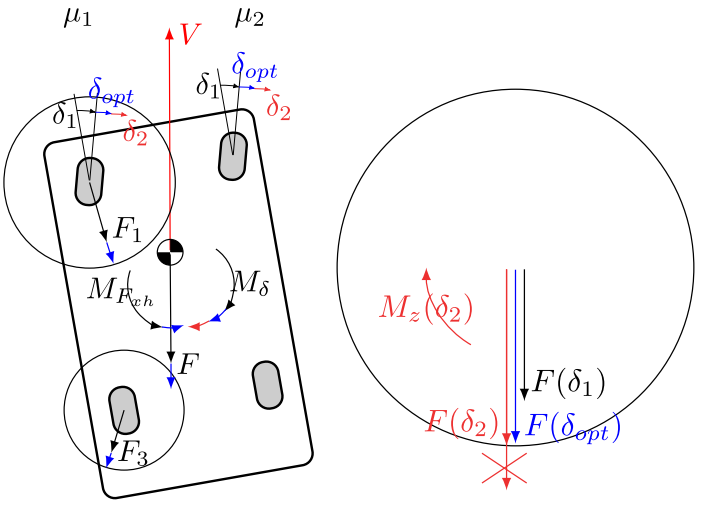

(a) Steering and braking torque contributions (b) Total force and friction limit

Figure 8. Schematics of the steering wheel angle's δ effect on the yaw torque M_z and total force F. (a) Steering and braking torque contributions (b) Total force and friction limit.

A fundamental aspect of a torque controller is that it must be able to generate torque in both directions to control yaw. This is illustrated in Figure 8, where the yaw torque balance M_z and total force F are studied for constant steering angles δ slightly larger and smaller than the optimal value. Three cases are identified in the figure:

(1) For the optimal steering wheel angle ($\delta = \delta_{opt}$), the vehicle brakes at its maximum, and the yaw torque generated by the steering is equal to the one obtained by the braking, i.e. there is a torque equilibrium. This is the optimal solution presented previously in Sections 4.1 and 4.2.
(2) For a larger steering angle ($\delta = \delta_2 > \delta_{opt}$), the steering gives a larger torque and a larger counter torque is required from the brakes. However, more braking is not possible as the tyre forces are on their friction limits. Therefore, the vehicle is not at a yaw torque equilibrium and could veer out-of-lane or become unstable.
(3) For a lower steering angle ($\delta = \delta_1 < \delta_{opt}$), the required braking to obtain a torque equilibrium is smaller than the maximum braking. Therefore, we can now obtain both a positive and a negative yaw torque to steer the vehicle if needed.

The above analysis shows that (a) how much braking can be applied depends on the provided steering wheel angle, and (b) the consequence of applying a larger-than-optimal steering angle is brake control action saturation, leading to a potentially unstable system. Inspired by this analysis, we propose a control strategy with constant steering and using braking as a control variable to obtain yaw stability. However, this strategy can only work if the steering angle is set to a value smaller than the optimal.

This section examined the combined optimal braking and steering as a function of the split friction magnitude. The optimal solution depends on several simplifications and

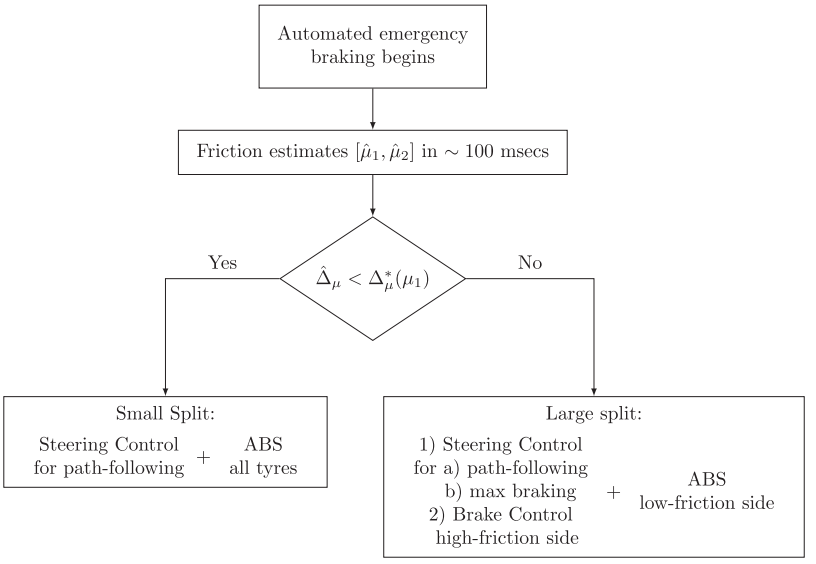

Figure 9. Control strategy and switch for large/small split friction asymmetry.

ignores dynamic responses, making it impractical to be directly realised. Instead, a control function is needed, which takes the steering and braking to the optimal values, i.e. to the static equilibrium and then keep the vehicle in that state for the whole brake manoeuvre.

5. Closed-loop control strategy

The control is described by three main measures: braking, yaw, and lateral positioning. The braking and yaw depend on the degree of split friction, and two different controllers are designed depending on Δ_μ. However, the lateral control is handled by a common path-following controller. The control strategy is presented in Figure 9 featuring the two control modes for large and small split friction asymmetry.

The switch between the two modes is performed by comparing the estimated friction asymmetry $\hat{\Delta}_\mu$ to $\Delta^*_\mu(\mu_1)$. For $\hat{\Delta}_\mu$, estimates of each vehicle side $[\hat{\mu}_1, \hat{\mu}_2]$ are needed, which become available after a few iterations of an estimation algorithm when braking hard, as in [15]. $\Delta^*_\mu(\mu_1)$ is obtained by solving offline the OP for a range of $[\mu_1, \mu_2]$ values as per Definition 4.1 and then arranging them into a lookup table.

The control strategy at small splits is straightforward, it combines the path-following controller with active ABS on all wheels, as depicted in Figure 10(a). Thanks to the ABS, all tyre forces remain close to their maximum values, recall Figure 5(a). $T_{bd,i}$ are the brake torque demands requested by the ABS. The path-following controller decides the steering δ_c, which provides the necessary counter torque, and keeps the lateral deviation errors small, assuming a look-ahead lateral distance measurement y_e exists in the vehicle. For more detailed approaches refer to [3–5].

The rest of the section describes, first, the common path-following controller, and second, the large-split brake controller.

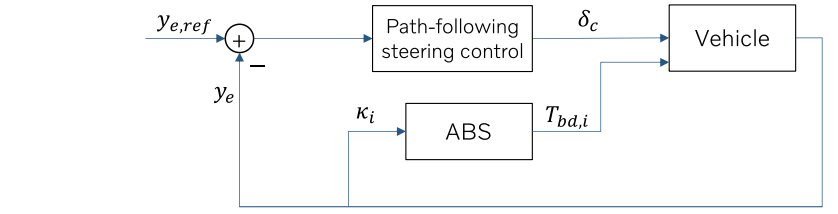

(a) Small split friction

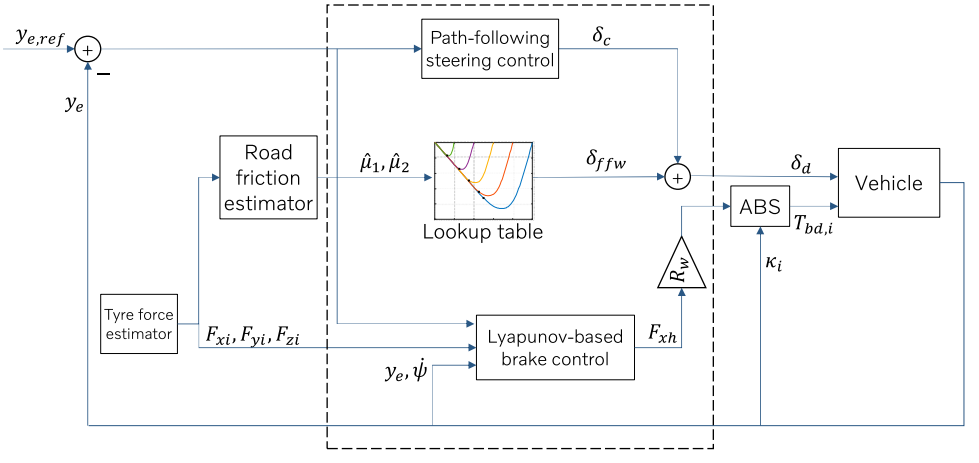

(b) Large split friction

Figure 10. Block diagrams of joint brake and steering control at small and large split friction asymmetries. (a) Small split friction (b) Large split friction.

5.1. Path-following controller

A lateral controller is needed to limit the lateral deviation during braking, created by the asymmetric brake forces and body slip angle in the initial braking stage.

The path deviation dynamics assuming a small yaw angle ψ are given by

$$\dot{e}_1 = v_x(\beta + e_2) \tag{32}$$

$$\dot{e}_2 = \dot{\psi} - \dot{\psi}_{des} \tag{33}$$

where e_1 is the distance of the CoG from the road centreline, e_2 is the orientation error, and ψ_{des} is a desired yaw angle, [10, Chapter 3]. The states are illustrated in Figure 1.

A look-ahead measurement is assumed to exist in the vehicle and is typically obtained from a vision system. The look-ahead distance is defined as

$$y_e = e_1 + d_s e_2 \tag{34}$$

where d_s is the longitudinal distance of the point ahead of the vehicle CoG at which the sensor measurement is made.

The position of the measurement d_s was studied in [10] for a linearised single-track model, with larger d_s values providing better damping. Here, a vision system is assumed,

which provides the measurement at $d_s = 10$ m. Using typical vehicle parameters, we found that a *PD* controller of the type

$$\delta_c = (k_p\, y_e + k_d\, \dot{y}_e) \tag{35}$$

with $k_p = 10\pi/180$ and $k_d = 0.05$ enhances the stability and greatly improves the phase margin of the linearised single-track model.

5.2. Control on large split

The proposed control strategy for large splits relies on a split friction estimate. Using this estimate, the steering angle is set to an offline-optimised value, while braking on the high-friction side is applied to control the yaw torque. Figure 10(b) presents the block diagram. It consists of three parts: (1) a feedforward steering angle, (2) a Lyapunov-based high-friction brake controller, and (3) the path-following steering controller from the previous subsection.

As presented in Figures 5(b)–7(b,c), the tyre forces on the low-friction side are in the sliding region. Hence, the control problem is simplified by disregarding their contribution. In contrast, almost all control action comes from the high-friction side. Controlling the high-friction brake forces F_{xh} ensures reducing the yaw torque based on the available steering torque. The inputs to this brake controller are yaw rate $\dot{\psi}$ and look-ahead lateral distance y_e measurements, and estimates of the brake and lateral forces. The high-friction brake controller is designed based on the Lyapunov theory, providing stability guarantees.

A basic ABS function is included in the design, i.e. the ABS engages only when excessive slip is detected and removes brake torque to reduce it. Here, it is used as a low-level controller on all wheels but is typically inactive on the high-friction side.

As discussed in Section 4.3, the steering wheel angle defines how much braking can be applied and whether the vehicle can be stabilised to zero yaw torque equilibrium. The steering controller consists of two parts: (i) constant feedforward steering angle δ_{ffw} obtained by a lookup table as a function of the split friction, and (ii) the *PD* controller from (35) to reduce path deviation errors, δ_c. The *total steering angle demand* is

$$\delta_d = \delta_{ffw} + \delta_c \tag{36}$$

Next, the construction of the lookup table for δ_{ffw} is presented.

5.2.1. Feedforward steering control for maximum braking on large splits

The feed-forward steering angle δ_{ffw} is determined by a lookup table, giving δ_{ffw} as a function of $\Delta_\mu(\mu_1)$, similarly to how Figure 6(b) is built. That is, the OP is solved offline with the vehicle parameters and for several friction coefficients as inputs, and its steering output is arranged into a lookup table. As discussed in Section 4.3, the steering wheel angle is chosen slightly less than the optimal one, enabling control action in both directions.

Closed-loop simulations in Section 7.2 show how close the vehicle comes to maximum braking when using the δ_{ffw} lookup table, as well as its sensitivity at extreme split friction asymmetries, where the LS and HsO solutions diverge.

5.2.2. Brake control on large split

The brake controller is based on Lyapunov theory and controls the high-friction brake forces to minimise yaw rate and deviations from the path.

The brake forces on each vehicle side are

$$F_{xh} = F_{x1} + F_{x3} \tag{37}$$

$$F_{xl} = F_{x2} + F_{x4} \tag{38}$$

where F_{xh} are the high-friction and F_{xl} the low-friction brake forces.

Choosing a constant front/rear axle brake ratio d_1, the high-friction brake forces are split into

$$\begin{cases} F_{x1} & = d_1 F_{xh}, \\ F_{x3} & = (1 - d_1) F_{xh} \end{cases} \tag{39}$$

Using the above in (8), the yaw torque M_z can be expressed as a linear function of F_{xh} in the form

$$M_z = A_{Mz} F_{xh} + B_{Mz} \tag{40}$$

where

$$A_{Mz} = -\frac{w}{2}$$

$$B_{Mz} = M_\delta + \frac{w}{2} F_{xl}$$

neglecting M_{cross} as it simplifies the derivation. It does not influence the closed-loop performance at large splits, as M_{cross} is much smaller than the other two torque components. In the closed-loop simulations (Section 7), M_{cross} is about 5% of the other torque components.

Inserting (40) into (14) the following is obtained

$$\ddot{\psi} = \frac{1}{I_{zz}} \left(A_{Mz} F_{xh} + B_{Mz} \right) \tag{41}$$

The Control-Lyapunov candidate [16] is selected as a quadratic function of a chosen error e, which will be defined below

$$V = \frac{1}{2} e^2 \tag{42}$$

The derivative of the error is defined as

$$\dot{e} = -k \frac{1}{2} e \tag{43}$$

for a tuning parameter $k > 0$. This control law will guarantee global exponential stability since substituting into the time derivative yields

$$\dot{V} = e\dot{e} = -kV < 0 \tag{44}$$

as V is positive definite.

The error is selected as a combination of a look-ahead path deviation distance measurement y_e and yaw rate $\dot{\psi}$ error as

$$e = a_0(0 - y_e) + a_1(\dot{\psi}_{des} - \dot{\psi}) \tag{45}$$

$$\dot{e} = a_1(0 - \ddot{\psi}) \tag{46}$$

where a_0, a_1 are tuning parameters for y_e and $\dot{\psi}$, respectively.

This gives a combined controller for the yaw and the path deviation. If it would not be included, the vehicle would have a lateral drift.

Inserting (41) into (46) gives the following error dynamics

$$\dot{e} = -a_1 \left(\frac{1}{I_{zz}} (A_{Mz} F_{xh} + B_{Mz}) \right) \tag{47}$$

which is then inserted into the Control-Lyapunov expression (43), solving for the total brake force on the high-friction side as

$$F_{xh} = A_{Mz}^{-1} \left[a_1^{-1} I_{zz} \frac{k}{2} e - B_{Mz} \right] \tag{48}$$

The brake forces F_{xh} are applied by the brakes by transforming the force into torque.

5.2.3. Measurements and estimates of the brake controller

There are two measurements needed to obtain e in F_{xh}: yaw rate $\dot{\psi}$ and a path deviation measurement y_e from (34). Further, a tyre force estimator is needed to estimate F_{xl} and M_δ in B_{Mz}. The brake forces F_{xl} can be estimated together with the lateral axle forces (obtaining M_δ) from [15], where longitudinal acceleration a_x, lateral acceleration a_y, and wheel speed ω_i measurements are required.

This section discussed control strategies to maximise deceleration, categorising them into two modes based on split friction magnitude. Next, we examine the relationship between steering and maximum braking in an experiment where a human driver handles the steering, highlighting the drawbacks on braking performance.

6. Baseline controller design from measurement

Some vehicles already have built-in features that assist with hard braking on split friction surfaces. Since the exact operation of these functions is unclear, an experiment was conducted to observe them in action.

6.1. Brake measurement with state-of-the-art function enabled

The test took place at Hällered Proving Grounds in the low-friction track. The track, made of basalt plates with a water-spraying system, had a friction coefficient of 0.2–0.3, while the areas outside had a coefficient of 0.7–0.8. A professional driver braked hard, placing the vehicle's left side on high friction and the right on low friction. The vehicle's ABS included a split friction function that offered steering recommendations. The already-prepared driver manoeuvred without relying on the system's steering recommendations, demonstrating optimal human performance.

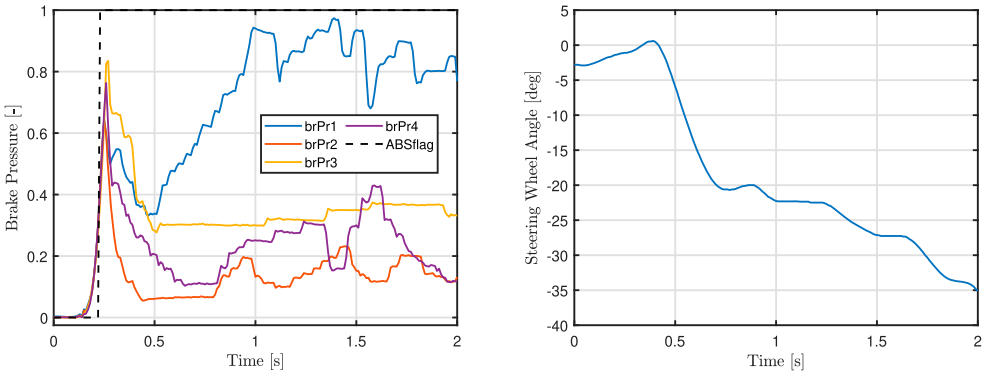

(a) Brake pressure for all wheels (b) Steering wheel angle

Figure 11. Split friction braking test data: first 2 seconds of braking. (a) Brake pressure for all wheels (b) Steering wheel angle.

Figure 11 presents the logged brake pressures and steering wheel angle for the first two seconds of the manoeuvre. Four phases can be identified in the build-up:

(1) Pressure increase [0.1–0.2 s]: The driver presses the brake pedal, and the pressure increases rapidly and equally on all wheels.
(2) Pressure decrease [0.2–0.4 s]: The ABS is activated, and soon after, brake pressure drops.
(3) Driver-brakes cooperative ramp-up [0.4–1 s]: Brake pressure and steering wheel angle are linearly increased. The split friction function ramps up the front high-friction brake pressure (blue line) as the driver counter-steers. The rear high-friction brake pressure remains constant (yellow line).
(4) Driver-brakes cooperative control [1–end s]: After reaching a desired brake pressure, smaller adjustments are made, where the driver controls the counter-steering, and the ABS controls the pressure in the wheels. The control continues until the vehicle stops.

It is evident that automating the steering can shorten phases 2 and 3. Further, there is a secondary benefit in increasing the rear high-friction tyre, as it remains constant here.

6.2. Emulating state-of-art split friction control

The experiment is used to create a baseline controller. Specifically, the driver's steering input in phases 2 and 3 is emulated as follows: (1) dead time for 0.2 s, (2) ramp for 0.6 s, and (3) automated steering afterwards. The Lyapunov-based controller (37) is chosen for the brake control, as it behaves similarly to the experiment. Hence, only the steering input in the first 0.8 s differs between the baseline and the proposed control. Still, since the brake control depends on the applied steering angle, the brake interventions will not be the same. This way, the effect of the driver's steering delay on the stopping distance and path deviation can be evaluated. A comparison of this baseline to the proposed optimal control design will be presented in Section 7.1.

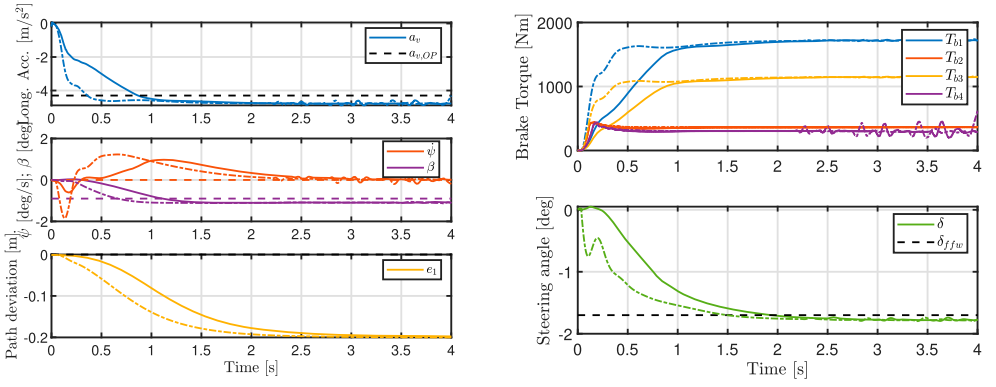

(a) Motion states (b) Inputs

Figure 12. Closed loop simulations (1) with baseline control emulating a professional driver (solid lines) and (2) with automated steering compensation (dash-dotted lines); OP targets with dashed lines for $\delta_{ffw} = -1.7^\circ$; $v_{x0} = 70$ km/h, $\Delta_\mu = 0.6 \mid \mu_1 = 0.8$. (a) Motion states (b) Inputs.

7. Closed-loop simulation results

The high-fidelity simulation environment CarMaker^{TM} (CM) is used for the closed-loop simulations. The dimensions and weight parameters of the vehicle are known. Still, the tyre models and the actuator properties are not, while the complete model includes the chassis, suspension dynamics, and other degrees of freedom, which were not considered in the presented double-track model.

The vehicle used in the CM simulations is a rear-wheel drive Polestar 2. The road is straight for every case. The virtual driver accelerates to a chosen speed and abruptly applies the brakes when reaching a specified distance. Section 7.1 presents the comparison using the driver and automated steering. Section 7.2 presents the sensitivity of the feedforward steering input with respect to the optimal braking equilibrium in closed-loop. Finally, Section 7.3 presents the controller's performance and limitations when braking without any friction on one vehicle side.

7.1. Comparison between automated steering and emulated driver

The emulated human driver from Section 6.2 and the fully automated steering compensation from Section 5.2 are compared in simulation.

Figure 12 presents the motion states and inputs. In the longitudinal acceleration of Figure 12(a), the $a_{v,OP}$ denotes the deceleration from the OP (29) with a $\delta_{ffw} = -1.7^\circ$, chosen slightly less than the optimal one (the optimal δ_{ffw} is discussed later in Figure 13). With the driver, the deceleration response follows the steering input from Figure 12(b). That is, the deceleration first increases up to -2 m/s^2 due to zero steering, thus momentarily converging to the low-friction side. Then, the deceleration rises at a similar rate as the steering angle. For the automated control, δ_{ffw} is applied almost instantly, but the steering quickly reverses due to the slower brake application, which leads to an increase in yaw rate. The yaw rate $\dot{\psi}$ converges to zero after 2 s, while the body slip angle β remains close to the target from the OP. The path deviation converges to a steady-state error of about -0.2 m.

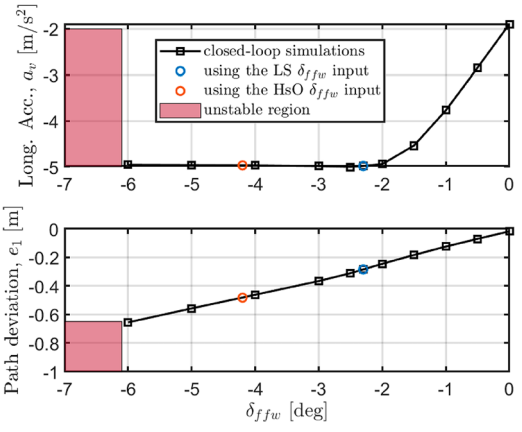

Figure 13. Deceleration and path deviation obtained at steady-state during closed-loop simulations as a function of a constant feedforward steering angle; blue/red circles denote the results using the δ_{ffw} for the LS/HsO solution, respectively; $v_{x0} = 70$ km/h, $\Delta_\mu = 0.6 \mid \mu_1 = 0.8$.

Table 1. Stopping distance comparison between automated steering and human driver.

Speed [km/h]	Stopping Distance [m]		Difference
50	25.5	22.3	−3.2 m, −13%
70	47.2	42.9	−4.3 m, −9%
90	75	69.7	−5.3 m, −7%
110	109	102.4	−6.6 m, −6%

The driver's steering delay impacts stopping distance, as shown in Table 1, with a greater effect at lower speeds. Since the results come from emulating a professional driver, prepared to counter-steer, we expect even longer stopping distances for an average driver.

7.2. Feedforward steering sensitivity to maximum braking in closed-loop

Figure 13 shows the sensitivity of the controller's feedforward steering angle δ_{ffw} to the converged deceleration and path deviation at steady-state. The figure is created after performing several closed-loop simulations in the same road condition and initial speed as in the previous section. The only change between each simulation is how much δ_{ffw} is applied.

When the δ_{ffw} is zero, the brake controller decelerates to 0.2 g– the same as the low-friction side coefficient μ_2– as the steering creates no counter-torque and the only option to reject the yaw torque disturbance is to make the brake forces equal per axle according to the low-friction side. Appendix provides the mathematical expression why. As $|\delta_{ffw}|$ increases, the deceleration also increases until reaching a plateau at about $|\delta_{ffw}| = 2.5^\circ$. Increasing the $|\delta_{ffw}|$ further gives no more deceleration, but the path deviation keeps increasing, up to the point of vehicle instability. Reducing the measurement distance d_s in (34) decreases the steady-state path deviation error but makes the closed-loop less stable (see [10]). However, the link between steering angle and path deviation persists, requiring reduced braking to restore manoeuvrability, as explained in Section 4.3.

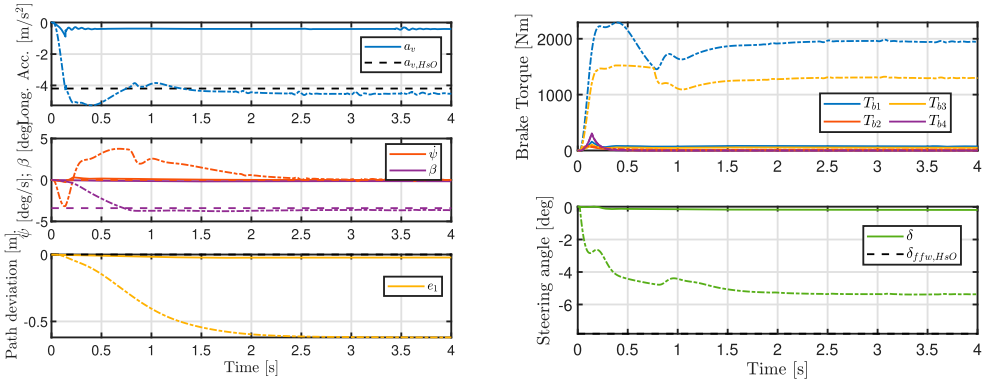

(a) States (b) Inputs

Figure 14. Black Ice: Closed loop simulation at almost zero friction on the right vehicle side. The simulation is performed for two different feedforward steering angles (1) $\delta_{ffw} = -0.1^\circ$ (solid lines) (2) $\delta_{ffw} = -5^\circ$ (dash-dotted lines); $v_{x0} = 70$ km/h, $\Delta_\mu = 0.99 \mid \mu_1 = 1$. (a) States (b) Inputs.

In the real vehicle, verging into the unstable region should be prevented typically by the ESP, when a combination of too large $\dot{\psi} - \beta$ are observed [14]. However, it is not in the scope of this paper to evaluate how the current controller interacts with an ESP algorithm.

These connections between steering, deceleration, and the lateral motion states are observed in the extreme case of zero friction on one vehicle side, coming next.

7.3. Control performance with zero friction on one vehicle side

The dynamic response of acceleration, yaw rate, and lateral deviation is studied in the special case of almost no friction on the right side of the vehicle. This scenario can occur due to black ice, typically forming around 0 °C when raining, or during aquaplaning. This example highlights the controller's limits and how adjustments can be made by tuning the lookup table.

The simulation is performed for two feedforward steering angles δ_{ffw} with the proposed control scheme, and the results are presented in Figure 14. For $\delta_{ffw} = -0.1^\circ$, obtained from the LS solution, the vehicle experiences low yaw rates and path deviations, but the deceleration achieved is small, about 0.4 m/s^2. Increasing the feedforward angle to $\delta_{ffw} = -5^\circ$ gives a deceleration as the HsO solution $a_{v,HsO} = 4.2$ m/s^2. For this increased δ_{ffw}, the initial transient of the yaw rate increases in magnitude and duration, and the path deviation increases to about -0.6 m. The side slip angle approaches the offline optimal solution. It is good to know that pushing the δ_{ffw} further leads to vehicle instability; the HsO solution here is $\delta_{ffw,HsO} = -7.8^\circ$ and thus unstable. As the friction asymmetry and the generated yaw torque are the maximum they can be, the vehicle is expected to be less stable, and a larger difference to the offline optimal solution is expected.

In fact, for this extreme case, using the ABS on all wheels or the in-built CM standard driver causes the vehicle to become unstable. It is thus safe to assume that an inexperienced driver with a traditional ABS will find it very hard to stabilise the vehicle and maintain it within the road bounds.

8. Discussion

The following insights summarise the simulation results:

- In conventional human-driven vehicles, steering can be pre-set based on a lookup table to assist the driver. This is especially important during the initial stages of braking, as yaw torque can be abrupt. Without timely counter-steering, the driver might be unprepared and veer out of the lane.
- Automating steering compensation results in 6–13% shorter stopping distances compared to a professional driver on the chosen split friction surface. This difference is due to the steering delay introduced by the human driver. Since the professional driver in the experiment was prepared to counter-steer, it is reasonable to assume that the stopping distance benefit would be even greater for an unprepared regular driver who takes longer to react.
- There is a relation between counter-steering and how much braking can be achieved. Increasing the steering angle reveals a trade-off between braking and path deviation. Further, pushing the steering angle too far can lead to vehicle instability, which depends on the generated yaw torque and body side slip angle.
- How close a control framework comes to minimum stopping distance mainly depends on two factors: (a) finding the maximum steady-state braking and counter-steering, and (b) shortening the transients before reaching this steady-state. Both factors rely on the effectiveness of the coordinated braking and steering control. The proposed optimisation framework of this paper focussed on the first point, which has not been sufficiently covered in previous literature.
- In this paper, we assume a flat, straight road, allowing the algorithm to neglect roll dynamics. However, it is fairly straightforward to extend the model to include roll dynamics and account for roll-dependent normal forces at the wheels due to road unevenness, such as during hill climbing.

9. Conclusion

Braking on split friction is dangerous due to abrupt yaw torque disturbance. The driver has to compensate by counter-steering, but if the driver is not quick enough at the beginning of braking, the vehicle can veer out of the lane. A straightforward solution is to automate steering compensation.

This paper proposes a static optimisation problem to maximise braking on split-friction roads without veering out of lane. The control problem is split into two cases: small and large friction asymmetry. For small splits, maximum braking is achieved by maximising individual tyre forces and applying counter-steering. For large splits, the high-friction tyres reach their force limit, while low-friction tyres slip beyond their peak. We show that limiting tyre slip reduces braking efficiency, and since the low-friction tyres contribute little, their torque can be disregarded, which enables focussing only on balancing high-friction braking and steering torque.

We introduce an optimal control framework bringing the vehicle to the static maximum braking. The traditional ABS and a path-following controller give maximum braking with

minor lateral deviations at small split friction asymmetries. However, at larger asymmetries, accurate counter-steering application is needed for maximum braking, a factor not thoroughly addressed in previous literature. Our approach uses (i) a feedforward steering angle from a lookup table and (ii) a high-friction braking controller that reduces excessive yaw torque. The simplicity of our control algorithm makes it easier to understand the main principles and limitations of combined braking and steering on split friction roads.

The proposed controller performs well in high-fidelity simulations, reaching the maximum static deceleration with minimal path deviation and quick yaw rate reduction. It is effective even with zero friction on one vehicle side. Additionally, automating steering improves stopping distance compared to an emulated human driver.

Future steps include resolving the steering-to-max braking connection with a slower outer loop that adjusts the steering wheel angle such that maximum braking is reached online. The online closed-loop optimisation results will then be compared to the simple solution of this paper. In-vehicle real-time tests will be conducted next.

Disclosure statement

Ektor Karyotakis and Derong Yang are employees of Volvo Car AB (Volvo Cars). Mats Jonasson is affiliated with Chalmers University of Technology and works part-time as a consultant for companies in Gothenburg, including Volvo Cars and Volvo Group. The authors declare no other financial or personal relationships that could have influenced the work reported in this paper.

Funding

This work was supported by (a) Volvo Car AB (Volvo Cars) and (b) Fordonsstrategisk forskning och innovation (FFI) [Strategic Vehicle Research and Innovation] part of Verket för Innovationssystem (VINNOVA) [2020-05169] [Swedish Innovation Agency].

ORCID

Ektor Karyotakis https://orcid.org/0000-0002-4568-0762
Mats Jonasson http://orcid.org/0000-0002-7385-5195

References

[1] National Center for Statistics and Analysis. Traffic safety facts 2020: a compilation of motor vehicle crash data. (Report No. DOT HS 813375). National Highway Traffic Safety Administration; 2022. Available from: https://crashstats.nhtsa.dot.gov/.
[2] Tagesson K, Jacobson B, Laine L. Driver response to automatic braking under split friction conditions. In: Proc. of the 12th International Symposium on Advanced Vehicle Control (AVEC); Tokyo, 2014. p. 666–671.
[3] Hebden RG, Edwards C, Spurgeon SK. Automotive steering control in a split-μ manoeuvre using an observer-based sliding mode controller. Veh Syst Dyn. 2004;41:181–202. doi: 10.1076/vesd.41.3.181.26511
[4] Yu L, Zheng S, Dai Y, et al. A feedback-feedforward steering controller designed for vehicle lane keeping in hard-braking manoeuvres on split-μ roads. Veh Syst Dyn. 2022;60:1763–1787. doi: 10.1080/00423114.2020.1869274
[5] Abi L, Jin D, Zheng S, et al. Dynamic coordinated control strategy of autonomous vehicles during emergency braking under split friction conditions. IET Intell Transp Syst. 2021;15:1215–1227. doi: 10.1049/itr2.v15.10

[6] Mirzaeinejad H, Mirzaei M, Kazemi R. Enhancement of vehicle braking performance on split-μ roads using optimal integrated control of steering and braking systems. Proc Inst Mech Eng, Part K: J Multi-body Dyn. 2016;230:401–415.
[7] Xue Z, Li C, Wang X, et al. Coordinated control of steer-by-wire and brake-by-wire for autonomous emergency braking on split-μ roads. IET Intell Transp Syst. 2020;14:2122–2132. doi: 10.1049/itr2.v14.14
[8] Karyotakis E, Jonasson M, Yang D, et al.. Minimizing stopping distance on split friction via steering and individual wheel braking optimization. In: Huang W, Ahmadian M, editors. Advances in Dynamics of Vehicles on Roads and Tracks III. IAVSD 2023. Lecture Notes in Mechanical Engineering. Cham: Springer. doi: 10.1007/978-3-031-66968-2_37
[9] Fors V, Nielsen L, Olofsson B. Models for optimization of vehicle maneuvers. Vehicular Systems, ISY, Linköping University; 2023.
[10] Rajamani R. Vehicle dynamics and control. 2nd ed. New York: Springer Science+Business Media; 2012. doi: 10.1007/978-1-4614-1433-9
[11] Pacejka H. Tire and vehicle dynamics. 3rd ed. Oxford, UK: Elsevier Ltd; 2012. doi: 10.1016/B978-0-08-097016-5.00001-2
[12] Jacobson B, Jonasson M, Bruzelius F. Compendium in vehicle motion engineering. Chalmers University of Technology; 2023.
[13] Petrescu RVV. Mechatronic systems to the braking mechanisms. J Mechatron Robot. 2020;4(1):156–190. doi: 10.3844/jmrsp.2020.156.190
[14] Van Zanten AT. Bosch ESP systems: 5 years of experience. SAE Trans. 2000;109:428–436. Section 7: Journal of Passenger Cars: Electronic and Electrical systems. Available from: https://www.jstor.org/stable/44699158?seq=6.
[15] Choi M, Oh JJ, Choi SB. Linearized recursive least squares methods for real-time identification of tire–road friction coefficient. IEEE Trans Veh Technol. 2013;62(7):2906–2918. doi: 10.1109/TVT.2013.2260190
[16] Khalil HK. Nonlinear control. Upper Saddle River, NJ: Pearson; 2015.

Appendix. High-friction brake control: special case of zero steering input

In the special case where there is no steering input, i.e. $\delta = 0$, and the road is straight, $\dot{\psi}_{des} = 0$, the sum of the brake forces on the high-friction side F_{xh} from (48) reduces to the sum of brake forces on the low-friction side F_{xl}

$$\begin{aligned} F_{xh} &= A_{Mz}^{-1}\left[a_1^{-1} I_{zz}\frac{k}{2}e - B_{Mz}\right] \\ &= -\frac{2}{w}\left[a_1^{-1} I_{zz}\frac{k}{2}e - \left(M_\delta + \frac{w}{2}F_{xl}\right)\right] \\ &= -\frac{2}{w}\left[a_1^{-1} I_{zz}\frac{k}{2}0 - \left(0 + \frac{w}{2}F_{xl}\right)\right] \\ &= F_{xl} \end{aligned}$$

As the error becomes zero at steady-state: $e = 0 \rightarrow [y_e, \dot{\psi}] = 0$, then $\beta = -\psi = 0$ from (32). Also, since $[\beta, \dot{\psi}] = 0$, the lateral slips are zero, as are the lateral forces, $F_{yi} = 0$, and consequently, $M_\delta = 0$. This solution gives a lower limit to the deceleration, $a_v = -\mu_2 g$, presented in Figure 4(a).